

Phase Transformations During Continuous Cooling in Inconel 718 Alloys Manufactured by Laser Powder Bed Fusion and Suction Casting

Yunhao Zhao, Liangyan Hao, Wei Xiong*

*Physical Metallurgy and Materials Design Laboratory,
Department of Mechanical Engineering and Materials Science,
University of Pittsburgh, Pittsburgh, PA 15261, USA*

** Corresponding Author, Email: weixiong@pitt.edu, w-xiong@outlook.com
Tel. +1 (412) 383-8092, Fax: +1 (412) 624-4846*

Abstract

Study on phase transformations in alloys during continuous cooling is important for post-processing design and optimization, especially for the additively manufactured (AM) alloys. In this work, continuous-cooling-transformation (CCT) diagrams for Inconel 718 manufactured by laser powder bed fusion (LPBF) and suction-casting are developed under different homogenization conditions. NbC carbides and δ phase are determined to be the main precipitates after cooling. Homogenization time and manufacturing methods are found to affect the Nb homogeneity in the alloys and thus further influence the precipitation process of the δ phase during cooling. In the alloys with high Nb homogeneity, the nucleation process mainly contributes to the precipitation, whereas in the alloys with low Nb homogeneity, the precipitation is promoted by the growth process. Subgrains are found to form after cooling at 0.1 K/s and can cause the highest hardness in samples. This work provides a new viewpoint on the study of processing-structure-property relationships during cooling in Inconel 718 and is beneficial to the development of alloy post-processing strategies.

Keywords: CCT diagrams; Inconel 718; additive manufacturing; phase transformations

1. Introduction

Inconel 718 is one of the most widely used superalloys in the aerospace industry because of its good strengthening property, oxidation resistance, and creep resistance at high service temperature [1–3]. In recent years, the application of Inconel 718 in additive manufacturing (AM) has also grown rapidly owing to its good weldability and the increasing demands for the high-temperature components with complex shapes [4–6]. Inconel 718 has an austenite matrix of γ (fcc_A1) phase and is precipitation-hardenable with the plate-shaped γ'' (Ni_3Nb , bct_D0₂₂) being the major strengthening phase, and sphere-shaped γ' ($\text{Ni}_3(\text{Al}, \text{Ti}, \text{Nb})$, fcc_L1₂) as the minor strengthening phase [7,8]. Besides, MC carbides (NbC, fcc_B1) usually form along with γ at high temperatures. δ (Ni_3Nb , D0₃) and Laves_C14 ((Ni, Fe, Cr)₂(Nb, Ti, Mo), hexagonal) are two detrimental intermetallic phases that are often observed in the alloy. δ phase has a needle shape and usually precipitates along grain boundaries [8,9]. It can pin the grain boundaries for grain size control but degrades strengthening property due to its incoherent phase boundary with γ [10]. Laves_C14 phase forms during solidification as a result of Nb at grain boundaries. To avoid crack initiation due to segregation, Inconel 718 alloys are often homogenized at elevated temperature as one of the most effective solutions [11,12].

It has been found that the phase transformation behaviors in Inconel 718 strongly depend on the applied heat treatments [13–15]. Therefore, for the alloys manufactured by traditional methods (such as casting) and novel methods, especially by AM approach, in which the builds experience

multiple heating and cooling cycles, understanding the microstructure evolution during the continuous cooling process is critical for the microstructure control, design and optimization of post-processing strategies [10,13,16–21]. The phase transformations during continuous cooling are usually illustrated by continuous-cooling-transformation (CCT) diagrams. A few CCT diagrams of Inconel 718 have been previously reported [13,22–24], as summarized in Fig. 1. Garcia et al. [13] used a dilatometer to investigate the effect of homogenizations at 1180°C for 24, 72, and 90 hours on the CCT diagrams of cast Inconel 718 alloys. They found the CCT curves shifted to the slower side of reaction with increased homogenization durations (Fig. 1(a)). The authors also reported that during cooling after 90-hour homogenization, new and small MC carbides formed before the δ phase, which was different from the cases of 24 and 72-hour homogenizations. This was explained as the Nb segregation along grain boundaries was reduced after long-time homogenization, which increased the Nb supersaturation within the grains and promoted the formation of MC carbides, but limited δ . However, the formation temperature of the δ phase was determined to be quite high (Fig. 1(c)), which is up to about 1130°C. This temperature is much higher than the reported solvus temperatures of δ from 998.3 to 1027°C obtained from experiments and CALPHAD (calculation of phase diagrams) calculations [25–28]. In addition, the Laves_C14 phase, γ'' , and γ' were also found to form after continuous cooling, as can be seen in Figs. 1(b),(d)&(e). γ'' was determined to precipitate prior to γ' during cooling. The critical cooling rates for γ'' were 1~10 K/s, depending on the homogenization time (Fig. 1(d)). Geng et al. [22] investigated the phase transformation behaviors of γ'' and δ during continuous cooling after homogenization at 1100°C for 1 hour in hot-extruded Inconel 718 alloys. They determined the γ'' precipitated under very slow cooling rates of 0.1~20 K/min (0.0017~0.33 K/s), while δ formed at cooling rates lower than 5 K/min (0.083 K/s). The result deviated a lot from [13]. Slama and Cizeron [23] reported only γ''/γ' precipitated during cooling, and the critical cooling rates were extremely high, as reproduced in Fig. 1(d). Niang et al. [24] provided a CCT curve for δ measured by differential thermal analysis (DTA) in forged Inconel 718 alloys, the critical cooling rate of δ was evaluated to be about 0.5 K/s (Fig. 1(c)).

Although some CCT diagrams of Inconel 718 have been reported, the results from different work are inconsistent and dependent on the alloy fabrication status. Moreover, the CCT diagrams of AM Inconel 718 still lack investigation, which may impede the post-processing development. The present work aims at studying the phase transformation behaviors during continuous cooling processes after different homogenizations in Inconel 718 alloys, which are made by laser powder bed fusion (LPBF) and suction-casting. The suction-cast alloys are chosen as a reference for comparison because they have comparative phase transformation behaviors during homogenization processes from AM alloys [29]. The CCT diagrams are established for each alloy based on the microstructure characterization and dilatometry analysis. The mechanical properties of the alloys after cooling are investigated, and mechanisms of microstructure and property evolution are also discussed.

2. Experiments and Simulation

2.1. Experiments

The AM alloys were built by an EOS M 290 machine using default building parameters, which are optimized for Inconel 718 by the company. The cast alloys were made by the suction-casting method using an arc-melter (ABJ-338, Materials Research Furnace Inc.) under Argon atmosphere to avoid oxidation. The nominal compositions of these two alloys are close, with Ni-18.26Fe-18.87Cr-4.97Nb-2.97Mo-0.94Ti-0.46Al-0.03C-0.06Mn-0.23Co-0.05Cu-0.06Si (in wt.%) for the

AM alloys, and Ni-18.5Fe-18.3Cr-4.99Nb-3.04Mo-1.02Ti-0.55Al-0.051C-0.23Mn-0.39Co-0.07Cu-0.08Si (in wt.%) for the suction-cast alloys, respectively. Both alloys were sectioned by EDM wire cutting into cuboids with a dimension of 4×4×10 mm for dilatometry measurements. The length (10 mm) of the cuboids of AM alloys is along their building directions.

The cuboid samples were subjected to dilatometry experiments with an S type thermocouple. For each alloy, two groups of samples were further divided with respect to different homogenization conditions, i.e., 1180°C for 20 min and for 12 hours, respectively. Samples of each group were then put into a quenching dilatometer (DIL805A, TA company) for the homogenization and subsequent cooling processes to room temperature. The cooling rates were 0.1, 1, 2, 5, 7, 10, and 15 K/s. The sample notations and heat treatment conditions in the present work are summarized in Table 1. It should be pointed out that for protecting the dilatometer, the samples to be homogenized for 12 hours were firstly encapsulated into quartz tubes with backfilled Argon and were then homogenized into the furnace at 1180°C for 11 hours. These 11-hour homogenized samples were then quenched into ice-water and put into the dilatometer for the remaining 1-hour homogenization at 1180°C. The continuous cooling processes were conducted on these samples subsequently.

By checking the similarity of the obtained dilatation curves, typical as-cooled samples were selected from each group for microstructure characterization. These samples were polished using metallographic methods for SEM (scanning electron microscopy, Zeiss Sigma 500 VP, Carl Zeiss AG) and EDS (Oxford Instruments plc) characterization. The samples were also etched using a solution of 50 mL C₃H₆O₃+30 mL HNO₃+2 mL HF to reveal the existence of Nb-rich γ'' and γ' phases [30]. Vickers hardness testing was performed using a Leco LM-800 tester under a 50 gf load for 10 seconds.

2.2. Simulation

In order to understand the phase stability in Inconel 718, the equilibrium and nonequilibrium step diagrams of Inconel 718 are plotted by Thermo-Calc software using the TCNI8 thermodynamic database, as shown in Figs. 2(a)&(b), respectively. It can be found that NbC carbide is stable up to 1300°C and can co-exist with γ during homogenization at 1180°C. δ and γ' are stable phases from Fig. 2(a), whereas γ'' is a metastable phase which can only be calculated by suspending the formation of the δ phase. According to some reports, γ'' can transform into the δ phase after long-time aging processes [31,32]. The calculated step diagrams can be used to preliminarily determine the precipitation sequence from dilatometry measurements.

3. Results and discussions

3.1. Microstructure characterization and dilatometry analysis

The CCT diagrams are determined by integrating the microstructure characterization and dilatometry analysis. The microstructures of samples were characterized to investigate the phase transformation that occurred during cooling, and the signals obtained from dilatation curves can be interpreted consequently. Sample AM12h-5 is taken as an example of the analysis, as demonstrated in Fig. 3. The SEM micrograph (Fig. 3(a)) on the longitudinal plane parallel to the building direction of sample AM12h-5 shows block-shaped NbC carbides and needle-shaped δ precipitates form along the grain boundaries of γ matrix. Neither γ'' nor γ' phase is observed in the etched sample AM12h-5, as their precipitation was suppressed by the fast cooling.

The starting and ending temperatures of phase transformations during continuous cooling are determined by the dilatometry analysis. As indicated by Fig. 3(b), the dilatation is plotted as a function of temperature. The slope changes in the dilatation curve represent the occurrence of phase transformation. Because of the small fraction (less than 1% in total) of the precipitates formed during cooling processes, the slope change of dilatation in this work is small, which may reduce the accuracy of the measurement of phase transformation temperature. Hence, the phase transformation temperatures are evaluated to correlate the inflection points obtained from the analysis on the second derivative of the dilatation curve.

From Fig. 2(a), as the NbC is stable at 1180°C with γ matrix, the formation of NbC carbides should have started during homogenization processes at 1180°C. The starting temperature of NbC carbides during the cooling process is not available, and only the ending temperature can be determined. In sample AM12h-5 (Fig. 3(b)), the ending temperature of NbC precipitation is determined to be 962°C at which the first slope change occurs. Similarly, the second change of the slope at 872°C is determined as the starting temperature of δ precipitation. The ending temperature of δ precipitation is determined as 776°C. When the phase transformation of δ finishes, the slope of the dilatation curve approaches a constant, resulting in a segment almost horizontal in the differential curve of dilatation. The phase transformation temperatures for the rest samples experiencing continuous cooling are determined using similar methods.

3.2. CCT diagrams of AM and suction-cast alloys

The CCT diagrams of Inconel 718 alloys with different homogenization durations and manufacturing methods are established by the methods proposed in section 3.1 and illustrated in Fig. 4. It can be found that the NbC and δ phases are the main precipitates during cooling. This is in contrast to the work from Garcia et al. [13], in which multiple phases were found to precipitate in sequence during cooling. It is worthwhile to be noted that the trace of nuclei of γ''/γ' can be only found in sample AM20m-01, as will be discussed in detail in section 3.5. This finding agrees with the results from Geng et al. [22], who reported γ'' will precipitate at cooling rates between 0.1~20 K/min (0.0017~0.33 K/s). Since the signal of the γ''/γ' nuclei formation is undetectable in the dilatation curve, and such phase transformation is not found at other cooling rates, the CCT curves of γ''/γ' are not given in Fig. 4.

The starting and ending curves of phase transformations are evaluated from dilatation datasets. When the cooling rates become extremely slow, namely the phase transformations are at equilibrium, the starting and ending temperatures approach each other and are close to the solvus temperature of the phase. In this work, the solvus temperatures of the δ phase for the AM and suction-cast alloys are calculated by the TCNI8 database as 1040°C and 1034°C, respectively. The experimental CCT curves are extrapolated to the solvus temperatures when the cooling rates become extremely slow (Figs. 4(a)&(b)).

In the present work, three characteristics of the CCT curves, as illustrated in Fig. 4(a), are proposed to describe the phase transformation behaviors: (1) starting temperature of the phase transformation; (2) formation range, which is defined as the difference between the starting temperature and ending temperature at one certain cooling rate; and (3) critical cooling rate, below which the phase transformation will happen. From Fig. 4, the phase transformation ending curves of NbC show a small difference in all CCT diagrams. These curves tend to lower temperature with a slower cooling rate because the longer heating durations from a slow cooling rate can promote the precipitation of NbC more sufficiently. However, a remarkable difference between CCT curves of δ phase in the

alloys under different homogenization durations and manufacturing methods can be observed, indicating these factors can have significant effects on the phase transformation of the δ phase during continuous cooling. Such effects will be discussed in detail in the following sections.

3.3. The effect of homogenization durations on the CCT diagrams of the δ phase

The effects of homogenization durations on the starting temperature, formation range, and critical cooling rate of the CCT curves of the δ phase in AM and suction-cast alloys are summarized in Table 2. As listed in Table 2, different homogenization durations have opposite effects on the characteristics of CCT curves within the alloys made by the same manufacturing methods.

Specifically, for the AM alloys, the CCT curve of alloy AM20m (homogenized for 20 min) has lower starting temperature and smaller formation range, but higher critical cooling rate, when compared with alloy AM12h (Table 2). Similarly, the different homogenization durations also have a reversed influence on the characteristics of the CCT curve in suction-cast alloys, as presented in Table 2. However, the critical cooling rates in the suction-cast alloys are found to be the exception as equal values are obtained. This may be because the difference between the critical cooling rates of alloys AC12h and AC20m is small, and the critical cooling rates of these alloys actually lie in the range of 10~15 K/s, making the difference unidentifiable in the present work.

It can be speculated that the different microstructures achieved from homogenizations should be the reason causing the various CCT diagrams. Zhao et al. [29] found the Nb homogeneity degrees in Inconel 718 can vary with different manufacturing methods and homogenization conditions. From Fig. 5, for AM alloys, the Nb homogeneity will decrease with extended homogenization durations (Figs. 5(a)&(b)), whereas in suction-cast alloys, the Nb homogeneity will decrease during longer time homogenization (Figs. 5(c)&(d)). As Nb is the main element for forming the δ phase, its homogeneity level can affect the nucleation and growth process during precipitation, and further determine the kinetics of the phase transformations.

The determination of the nucleation rate N_r in this work is based on the classical nucleation theory [33,34]. Assume the nucleation process is steady, N_r is expressed as

$$N_r = Z\beta^*N_0\exp\left(-\frac{\Delta G^*}{k_B T}\right) \quad 1$$

where Z is the Zeldovich factor, which gives the probability of a nucleus to form a new phase, β^* is the attachment rate of atoms to the critical nucleus, N_0 is the number of potential nucleation sites of δ , ΔG^* is the nucleation barrier, k_B is the Boltzmann constant, T is temperature. From eq. 1, it can be deduced that increasing N_0 and decreasing ΔG^* are the two ways to increase the nucleation rate.

Except for the nucleation rate, the growth rate can also affect the precipitation kinetics. The growth rate of δ particle J_r is expressed by [35]

$$J_r = \frac{\Delta X_0^{Nb}}{2(X_\delta^{Nb} - X_e^{Nb})} \left(\frac{D}{t}\right)^{\frac{1}{2}} \quad 2$$

of which $\Delta X_0^{Nb} = X_0^{Nb} - X_e^{Nb}$ is the supersaturation of Nb in the matrix, X_0^{Nb} is the Nb concentration in the matrix, X_e^{Nb} is the Nb equilibrium concentration in the matrix adjacent to the δ particles. X_δ^{Nb} is the Nb concentration in equilibrium δ phase, D and t are the interdiffusion

diffusivity and diffusion time, respectively. From eq. 2, it is deduced that when the supersaturation ΔX_0^{Nb} increases, the growth rate J_r is increased.

According to the analysis above, it is critical to comprehend how the Nb homogeneity influence the nucleation rate N_0 , nucleation barrier ΔG^* , the supersaturation ΔX_0^{Nb} to determine their effects on precipitation kinetics. Figure 6 takes the comparison between alloys AM20m and AM12h as an example to illustrate the way Nb homogeneity affecting the precipitation kinetics. As shown in Fig. 6, the homogenized sample AM20m has higher Nb homogeneity than sample AM12h, so each Nb atom in sample AM20m shares the same probability of becoming the potential nucleation site, which increases N_0 , and the nucleation rate N_r in eq. 1 rises accordingly. Nevertheless, the relatively high Nb homogeneity around the nuclei leads X_0^{Nb} in eq. 2 to be low as the concentration fluctuation of Nb will be negligible. The supersaturation ΔX_0^{Nb} in eq. 2 is hence reduced, resulting in a decrease in the growth rate. Thus, it can be deduced that the precipitation of the δ phase in alloy AM20m during continuous cooling is promoted by the nucleation process while limited by the growth process.

From eq. 1, the nucleation rate N_r can be increased significantly by lowering the nucleation barrier ΔG^* , which can be achieved by increasing the supercooling during the nonequilibrium cooling process. In alloy AM20m, the starting temperature of the CCT curve of δ is found to be lower than that in AM12h, as shown in Table 2 and the CCT diagram in Fig. 6. It confirms alloy AM20m has a larger supercooling degree during cooling when the δ phase starts to form, which is beneficial to the nucleation process. In addition, when the cooling rates for AM20m become faster, the supercooling of δ precipitation further increases, and a larger driving force of the nucleation process is provided. Because the precipitation in alloy AM20m is promoted by the nucleation process, a larger cooling rate is hence preferred for the phase transformation. This allows the δ phase to form at high cooling rates, which explains the higher critical cooling rate observed for the δ phase in alloy AM20m (Table 2 and CCT diagram in Fig. 6). In contrast, since the growth process of the δ phase is limited in alloy AM20m during cooling, the precipitation process finishes faster, leaving a relatively smaller formation range (Table 2).

In alloy AM12h, as can be seen in Fig. 6, due to the lower Nb homogeneity, the number of potential nucleation sites N_0 is less, as the Nb atoms close to the center of the Nb-rich area are more probable to become the nucleation sites. However, the local supersaturation around the nuclei can be higher. The growth process becomes the promoting factor of the precipitation, while the nucleation process limits the phase transformation. The precipitation kinetics of δ depends more on the precipitate growth in alloy AM12h during cooling. Under such circumstances, a small supercooling degree is beneficial to the diffusion of solute atoms during the growth process. Accordingly, in experiments, the CCT curve of the δ phase in alloy AM12h has smaller supercooling, leading to higher starting temperature comparing with that in alloy AM20m. The growth process in alloy AM12h can also last a longer time, and the formation range is thus larger (Table 2). In addition, when the cooling rates become higher in alloy AM12h, the phase transformation will be suppressed due to the diffusion of solute atoms is retarded, causing a lower critical cooling rate 7 K/s (Table 2 and Fig. 6).

For the suction-cast alloys AC12h and AC20m, a similar explanation on the difference of the CCT curves can be applied. As can be seen in Figs. 5(c)&(d), Nb homogeneity increases with longer homogenization durations, so alloy AC12h has higher Nb homogeneity than alloy AC20m. According to the analysis above, for suction-cast alloys homogenized for 20 min, the growth

process dominates the precipitation process of δ phase, while for suction-cast alloys homogenized for 12 hours, the nucleation process dominates the precipitation kinetics of δ phase. However, in the AM alloys, the effect of the homogenization duration on the precipitation kinetics is opposite to that in the suction-cast alloys. The explanations of how homogenization durations affect CCT curves of the δ phase in AM and suction-cast alloys are summarized in Table 3.

In summary, with the same manufacturing method, the homogenization durations can affect the phase transformation behaviors of the δ phase during continuous cooling processes. This effect is achieved by varying the Nb homogeneity. For AM alloys, extending the homogenization duration leads to the reduction of Nb homogeneity, making the precipitation kinetics of δ phase depends more on the growth process, yet for suction-cast alloys, the extension of homogenization durations results in an increase of Nb homogeneity, and the precipitation kinetics mainly depends on nucleation process.

3.4. The effect of manufacturing methods on the CCT diagrams of the δ phase

The manufacturing methods are also found to influence the precipitation of the δ phase in the alloys subjected to the same homogenization durations. As shown in Fig. 4(c)&(d) and listed in Table 4, with the same homogenization duration of 20 min (Fig. 4(c)), the CCT curve of δ phase in the AM alloy (AM20m) has lower starting temperature, smaller formation range, but higher critical cooling rate compared with the suction-cast alloy (AC20m). However, under homogenization for 12 hours (Fig. 4(d)), the AM alloy (AM12h) has a higher starting temperature, larger formation range, but a lower critical cooling rate than the suction-cast alloy (AC12h).

The observation on these characteristics of CCT curves suggests the manufacturing methods influence the precipitation kinetics during cooling. Adopting the analysis based on the Nb homogeneity evolution proposed in section 3.3, such difference can be readily interpreted. Figures 5(a)&(c) indicate alloy AM20m has higher Nb homogeneity than alloy AC20m; therefore, it can be inferred that the nucleation process is the main factor contributing to the precipitation of δ phase in AM20m. The supercooling degree in alloy AM20m should thus be large to provide sufficient nucleation driving force, which causes the reduction of starting temperature and increased critical cooling rate, as listed in Table 5. Meanwhile, the growth rate in AM20m is limited, attributed to lower Nb supersaturation, which leads to the smaller formation range. The effects of manufacturing methods on the CCT curves of samples homogenized for 12 hours listed in Table 4 can be interpreted in the same way, and the explanation is summarized in Table 5.

In general, with the same homogenization durations, the manufacturing methods can influence the precipitation kinetics of the δ phase during continuous cooling by generating different Nb homogeneity. For the short duration of homogenization (20 min), the AM alloy has higher Nb homogeneity, and the precipitation kinetics of the δ phase depends more on the nucleation process, yet the Nb homogeneity is lower in the suction-cast alloy, and the precipitation is more dependent on the growth process. The circumstances for long durations of homogenization (12 hours) are reversed.

3.5. The effect of cooling rate on the hardness properties

The hardness properties of the alloys after continuous cooling are investigated by Vickers microhardness testing, and the results are presented in Fig. 7. For the tested alloys, as illustrated in Fig. 7(a)-(d), the cooling rates of 1~15 K/s result in comparable hardness values (229.5 HV_{0.05} to 272.1 HV_{0.05}) with the as-homogenized samples. However, the hardness values achieved in the 0.1

K/s-cooled samples are evidently high. Sample AM20m-01 is found to own the highest hardness value of 421.1 HV_{0.05}, whereas the hardness values of the rest three samples cooled at 0.1 K/s vary from 349.8 HV_{0.05} to 402.8 HV_{0.05}. This finding suggests some significant changes in microstructures have occurred in these samples.

The precipitation of γ''/γ' strengthening phases may be one probable reason for the high hardness. Therefore, the four samples cooled at 0.1 K/s were etched to investigate if γ''/γ' precipitates exist. The microstructures are shown in Fig. 8. In sample AM20m-01, as shown in the subfigure of Fig. 8(a), a trace of γ''/γ' nuclei is observed. In contrast, in Figs. 8(b)-(d), no γ''/γ' nuclei can be observed in samples AM12h-01, AC20m-01, and AC12h-01. Since the samples cooled at 0.1 K/s all have relatively high hardness (Fig. 7), it can be concluded that γ''/γ' is not the reason contributing to the prevalent hardness increase. The exclusive precipitation of γ''/γ' in sample AM20m-01 is probably because the homogenized alloy AM20m has the largest amount of Nb dissolved into the matrix, as the least amount of Nb-rich phases (i.e., Laves_C14 and NbC carbides) was found in this alloy [29]. This leads to higher Nb concentration in the γ matrix compared with other homogenized alloys and makes the γ''/γ' precipitation readily.

In the etched microstructures, a large number of δ precipitates can be found to form along grain boundaries in all samples cooled at 0.1 K/s, as seen in the subfigures of Figs. 8(a)-(d). Moreover, the appearance of subgrain boundaries is observed in all 0.1 K/s-cooled samples (Fig. 8), which has not yet been reported in the previous studies. Such subgrain boundaries are not observed in the samples cooled at higher rates, which implies they may be related to the high hardness in the 0.1 K/s-cooled samples. The subgrains probably form through the tangling of dislocations, which are generated through the loss of coherency of δ/γ phase boundaries during the precipitation of the δ phase [36,37]. The δ particles can further pin the subgrain boundaries and regard their movement. As a result, small subgrains form due to the δ precipitation, and the hardness is elevated accordingly. Conversely, precipitation of the δ phase is limited at cooling rates faster than 0.1 K/s, so the subgrains are less likely to form. This explains the lower hardness obtained in the rest as-cooled samples. It should be noted that due to the formation of γ''/γ' nuclei in sample AM20m-01, the hardness is further increased compared with the rest 0.1 K/s cooled samples, as illustrated in Fig. 7(a).

Conclusions

1. The CCT diagrams of AM and suction-cast Inconel 718 alloys after homogenizations at 1180°C for 20 min and 12 hours are established based on microstructure characterization and dilatometry analysis. NbC carbides and δ phase are found to precipitate during continuous cooling process in all alloys at appropriate cooling rates.
2. Both homogenization durations and manufacturing methods can affect the phase transformation behaviors of the δ phase during cooling by changing the Nb homogeneity. The precipitation kinetics of the δ phase during cooling depends more on the nucleation process in alloys with higher Nb homogeneity, while the growth process is predominant in alloys with lower Nb homogeneity.
3. Compared with the samples cooled at higher rates, 0.1 K/s cooling rate can achieve the highest hardness in all alloys with different homogenization durations and manufacturing conditions. This is probably due to the formation of subgrains as a result of the abundant precipitation of the δ phase.

4. Compared with other samples cooled at 0.1 K/s, the hardness of the sample AM20m-01 is further increased due to the presence of γ''/γ' nuclei.

Acknowledgment

The authors thank the National Aeronautics and Space Administration for the financial support under the Grant Number (NNX17AD11G). We are also grateful for the Thermo-Calc company on the software and databases provided for CALPHAD modeling. Miss. Yinxuan Li is appreciated for the help of sample preparation.

Reference

- [1] E. Chlebus, K. Gruber, B. Kuźnicka, J. Kurzac, T. Kurzynowski, Effect of heat treatment on the microstructure and mechanical properties of Inconel 718 processed by selective laser melting, *Mater. Sci. Eng. A.* 639 (2015) 647–655. <https://doi.org/10.1016/j.msea.2015.05.035>.
- [2] X. Zhao, J. Chen, X. Lin, W. Huang, Study on microstructure and mechanical properties of laser rapid forming Inconel 718, *Mater. Sci. Eng. A.* 478 (2008) 119–124. <https://doi.org/10.1016/j.msea.2007.05.079>.
- [3] M.M. Kirka, F. Medina, R. Dehoff, A. Okello, Mechanical behavior of post-processed Inconel 718 manufactured through the electron beam melting process, *Mater. Sci. Eng. A.* 680 (2017) 338–346. <https://doi.org/10.1016/j.msea.2016.10.069>.
- [4] T. Trosch, J. Strößner, R. Völkl, U. Glatzel, Microstructure and mechanical properties of selective laser melted Inconel 718 compared to forging and casting, *Mater. Lett.* 164 (2016) 428–431. <https://doi.org/10.1016/j.matlet.2015.10.136>.
- [5] D. Zhang, Z. Feng, C. Wang, W. Wang, Z. Liu, W. Niu, Comparison of microstructures and mechanical properties of Inconel 718 alloy processed by selective laser melting and casting, *Mater. Sci. Eng. A.* 724 (2018) 357–367. <https://doi.org/10.1016/j.msea.2018.03.073>.
- [6] P. Han, Additive design and manufacturing of jet engine parts, *Engineering.* 3 (2017) 648–652. <https://doi.org/10.1016/J.ENG.2017.05.017>.
- [7] S.J. Hong, W.P. Chen, T.W. Wang, A diffraction study of the γ'' phase in INCONEL 718 superalloy, *Metall. Mater. Trans. A.* 32 (2001) 1887–1901. <https://doi.org/10.1007/s11661-001-0002-4>.
- [8] Y. Huang, T.G. Langdon, The evolution of delta-phase in a superplastic Inconel 718 alloy, *J. Mater. Sci.* 42 (2007) 421–427. <https://doi.org/10.1007/s10853-006-0483-z>.
- [9] S. Azadian, L.Y. Wei, R. Warren, Delta phase precipitation in inconel 718, *Mater. Charact.* 53 (2004) 7–16. <https://doi.org/10.1016/j.matchar.2004.07.004>.
- [10] W.J. Sames, K.A. Unocic, R.R. Dehoff, T. Lolla, S.S. Babu, Thermal effects on microstructural heterogeneity of Inconel 718 materials fabricated by electron beam melting, *J. Mater. Res.* 29 (2014) 1920–1930. <https://doi.org/10.1557/jmr.2014.140>.
- [11] M.J. Sohrabi, H. Mirzadeh, M. Rafiei, Solidification behavior and Laves phase dissolution during homogenization heat treatment of Inconel 718 superalloy, *Vacuum.* 154 (2018) 235–243. <https://doi.org/10.1016/j.vacuum.2018.05.019>.

- [12] M. Rafiei, H. Mirzadeh, M. Malekan, M.J. Sohrabi, Homogenization kinetics of a typical nickel-based superalloy, *J. Alloys Compd.* 793 (2019) 277–282. <https://doi.org/10.1016/j.jallcom.2019.04.147>.
- [13] C.I. Garcia, A.K. Lis, E.A. Loria, A.J. DeArdo, Thermomechanical processing and continuous cooling transformation behavior of IN-718, in: *Superalloys 1992 (Seventh Int. Symp., TMS, 1992: pp. 527–536*. https://doi.org/10.7449/1992/Superalloys_1992_527_536.
- [14] W.M. Tucho, V. Hansen, Characterization of SLM-fabricated Inconel 718 after solid solution and precipitation hardening heat treatments, *J. Mater. Sci.* 54 (2019) 823–839. <https://doi.org/10.1007/s10853-018-2851-x>.
- [15] W. Huang, J. Yang, H. Yang, G. Jing, Z. Wang, X. Zeng, Heat treatment of Inconel 718 produced by selective laser melting: microstructure and mechanical properties, *Mater. Sci. Eng. A.* 750 (2019) 98–107. <https://doi.org/10.1016/j.msea.2019.02.046>.
- [16] Y. Tian, D. McAllister, H. Colijn, M. Mills, D. Farson, M. Nordin, S. Babu, Rationalization of microstructure heterogeneity in INCONEL 718 builds made by the direct laser additive manufacturing process, *Metall. Mater. Trans. A.* 45 (2014) 4470–4483. <https://doi.org/10.1007/s11661-014-2370-6>.
- [17] S. Malinov, Z. Guo, W. Sha, A. Wilson, Differential scanning calorimetry study and computer modeling of $\beta \Rightarrow \alpha$ phase transformation in a Ti-6Al-4V alloy, *Metall. Mater. Trans. A.* 32 (2001) 879–887. <https://doi.org/10.1007/s11661-001-0345-x>.
- [18] C. Radhakrishna, K.P. Rao, S. Srinivas, Laves phase in superalloy 718 weld metals, *J. Mater. Sci. Lett.* 14 (1995) 1810–1812. <https://doi.org/10.1007/BF00271015>.
- [19] I. Yadroitsev, P. Krakhmalev, I. Yadroitsava, Hierarchical design principles of selective laser melting for high quality metallic objects, *Addit. Manuf.* 7 (2015) 45–56. <https://doi.org/10.1016/j.addma.2014.12.007>.
- [20] X. Hu, A. Nycz, Y. Lee, B. Shassere, S. Simunovic, M. Noakes, Y. Ren, X. Sun, Towards an integrated experimental and computational framework for large-scale metal additive manufacturing, *Mater. Sci. Eng. A.* 761 (2019) 138057. <https://doi.org/10.1016/j.msea.2019.138057>.
- [21] Y. Zhou, S. Chen, X. Chen, T. Cui, J. Liang, C. Liu, The evolution of bainite and mechanical properties of direct laser deposition 12CrNi2 alloy steel at different laser power, *Mater. Sci. Eng. A.* 742 (2019) 150–161. <https://doi.org/10.1016/j.msea.2018.10.092>.
- [22] L. Geng, Y. Na, N.-K. Park, Continuous cooling transformation behavior of Alloy 718, *Mater. Lett.* 30 (1997) 401–405. [https://doi.org/10.1016/S0167-577X\(96\)00225-X](https://doi.org/10.1016/S0167-577X(96)00225-X).
- [23] C. Slama, G. Cizeron, Étude du comportement structural de l'alliage NC 19 Fe Nb (Inconel 718), *J. Phys. III.* 7 (1997) 665–688. <https://doi.org/10.1051/jp3:1997148>.
- [24] A. Niang, B. Viguier, J. Lacaze, Some features of anisothermal solid-state transformations in alloy 718, *Mater. Charact.* 61 (2010) 525–534. <https://doi.org/10.1016/j.matchar.2010.02.011>.
- [25] J.W. Brooks, P.J. Bridges, Metallurgical stability of Inconel Alloy 718, in: *Superalloys 1988 (Sixth Int. Symp., TMS, 1988: pp. 33–42*.

https://doi.org/10.7449/1988/Superalloys_1988_33_42.

- [26] A. Oradei-Basile, J.F. Radavich, A current T-T-T diagram for wrought Alloy 718, in: *Superalloys 718, 625 Var. Deriv.*, TMS, 1991: pp. 325–335. https://doi.org/10.7449/1991/Superalloys_1991_325_335.
- [27] L. Yang, K. Chang, S. Mannan, I.A. International, A new DTA approach for verifying precipitate solvus in Inconel Alloy 718, *Superalloys 718, 625, 706 Var. Deriv.* (1997) 353–365.
- [28] X. Xie, C. Xu, G. Wang, J. Dong, W. Di Cao, R. Kennedy, TTT diagram of a newly developed nickel-base superalloy-Allvac® 718Plus™, *Proc. Int. Symp. Superalloys Var. Deriv.* (2005) 193–202. https://doi.org/10.7449/2005/superalloys_2005_193_202.
- [29] Y. Zhao, K. Li, M. Gargani, W. Xiong, A Comparative Analysis of Inconel 718 Made by Additive Manufacturing and Suction Casting: Microstructure Evolution in Homogenization, Unpublished.
- [30] Standard Practice for Microetching Metals and Alloys ASTM E-407, 07 (2016) 1–22. <https://doi.org/10.1520/E0407-07R15E01.2>.
- [31] Z. Chen, R.L. Peng, J. Moverare, P. Avdovic, J.M. Zhou, S. Johansson, Surface integrity and structural stability of broached Inconel 718 at high temperatures, *Metall. Mater. Trans. A.* 47 (2016) 3664–3676. <https://doi.org/10.1007/s11661-016-3515-6>.
- [32] Y.T. Chen, A.C. Yeh, M.Y. Li, S.M. Kuo, Effects of processing routes on room temperature tensile strength and elongation for Inconel 718, *Mater. Des.* 119 (2017) 235–243. <https://doi.org/10.1016/j.matdes.2017.01.069>.
- [33] K.C. Russell, Nucleation in solids: the induction and steady state effects, *Adv. Colloid Interface Sci.* 13 (1980) 205–318. [https://doi.org/10.1016/0001-8686\(80\)80003-0](https://doi.org/10.1016/0001-8686(80)80003-0).
- [34] J. Svoboda, F.D. Fischer, P. Fratzl, E. Kozeschnik, Modelling of kinetics in multi-component multi-phase systems with spherical precipitates I: Theory, *Mater. Sci. Eng. A.* 385 (2004) 166–174. <https://doi.org/10.1016/j.msea.2004.06.018>.
- [35] D.A. Poster, K.E Easterling, Precipitation Growth, in: *Phase Transform. Met. Alloy.*, 2nd ed., Chapman & Hall, 1992: p. 281.
- [36] M. Sundararaman, P. Mukhopadhyay, S. Banerjee, Precipitation of the δ -Ni₃Nb phase in two nickel base superalloys, *Metall. Trans. A.* 19 (1988) 453–465. <https://doi.org/10.1007/BF02649259>.
- [37] T. Omori, T. Kusama, S. Kawata, I. Ohnuma, Y. Sutou, Y. Araki, K. Ishida, R. Kainuma, Abnormal Grain Growth Induced by Cyclic Heat Treatment, *Science.* 341 (2013) 1500–1502. <https://doi.org/10.1126/science.1238017>.

Tables and Figures

Table 1. Sample notations and heat treatment conditions in the present work.

AM-LPBF ^a			Suction-casting		
Sample notation	Homogenization	Cooling rate, K/s	Sample notation	Homogenization	Cooling rate, K/s
AM20m-01	1180°C for 20 min	0.1	AC20m-01	1180°C for 20 min	0.1
AM20m-1		1	AC20m-1		1
AM20m-2		2	AC20m-2		2
AM20m-5		5	AC20m-5		5
AM20m-7		7	AC20m-7		7
AM20m-10		10	AC20m-10		10
AM20m-15		15	AC20m-15		15
AM12h-01	1180°C for 12 hours	0.1	AC12h-01	1180°C for 12 hours	0.1
AM12h-1		1	AC12h-1		1
AM12h-2		2	AC12h-2		2
AM12h-5		5	AC12h-5		5
AM12h-7		7	AC12h-7		7
AM12h-10		10	AC12h-10		10
AM12h-15		15	AC12h-15		15

^aAM-LPBF: Additive Manufacturing-Laser Powder Bed Fusion

Table 2. Summary of the effects of homogenization durations on the CCT characteristics of δ phase.

AM-LPBF	Homogenization durations	Starting temperature	Formation range	Critical cooling rate
AM20m	20 min	low	small	high
AM12h	12 hours	high	large	low
Suction-casting	Homogenization durations	Starting temperature	Formation range	Critical cooling rate
AC20m	20 min	high	large	equal
AC12h	12 hours	low	small	equal

Table 3. Summary of the explanations to the effects of homogenization durations on the CCT characteristics of δ phase.

AM-LPBF	Homogenization durations	Nb homogeneity	Nucleation potency/ Growth rate	Supercooling	Starting temperature	Formation range	Critical cooling rate
AM20m	20 min	high	high/low	large	low	small	high
AM12h	12 hours	low	low/high	small	high	large	low
Suction-casting	Homogenization durations	Nb homogeneity	Nucleation potency/ Growth rate	Supercooling	Starting temperature	Formation range	Critical cooling rate
AC20m	20 min	low	low/high	small	high	large	equal
AC12h	12 hours	high	high/low	large	low	small	equal

Table 4. Summary of the effects of manufacturing methods on the CCT characteristics of δ phase.

20 min homogenization	Manufacturing methods	Starting temperature	Formation range	Critical cooling rate
AM20m	AM-LPBF	low	small	high
AC20m	Suction-casting	high	large	low
12 hours homogenization	Manufacturing methods	Starting temperature	Formation range	Critical cooling rate
AM12h	AM-LPBF	high	large	low
AC12h	Suction-casting	low	small	high

Table 5. Summary of the explanations to the effects of manufacturing methods on the CCT characteristics of δ phase.

20 min homogenization	Manufacturing methods	Nb homogeneity	Nucleation potency/ Growth rate	Supercooling	Starting temperature	Formation range	Critical cooling rate
AM20m	AM-LPBF	high	high/low	large	low	small	high
AC20m	Suction-casting	low	low/high	small	high	large	low
12 hours homogenization	Manufacturing methods	Nb homogeneity	Nucleation potency/ Growth rate	Supercooling	Starting temperature	Formation range	Critical cooling rate
AM12h	AM-LPBF	low	low/high	small	high	large	low
AC12h	Suction-casting	high	high/low	large	low	small	high

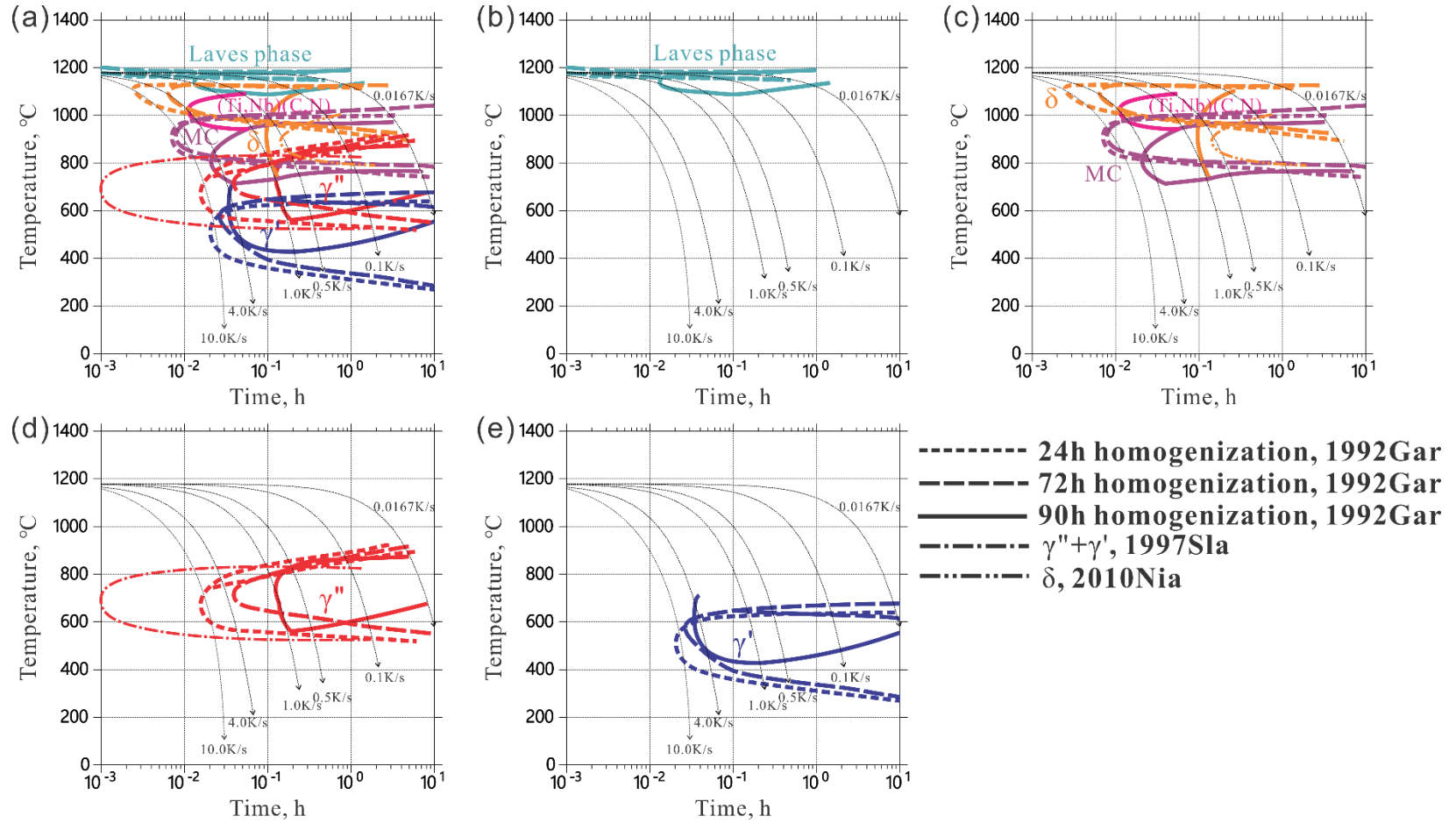


Figure 1. Review of CCT diagrams reported in the literature. (a) Integrated CCT diagrams; (b) CCT diagrams of the Laves phase; (c) CCT diagrams of the δ phase and MC carbides; (d) CCT diagrams of the γ'' phase; and (e) CCT diagrams of the γ' phase.

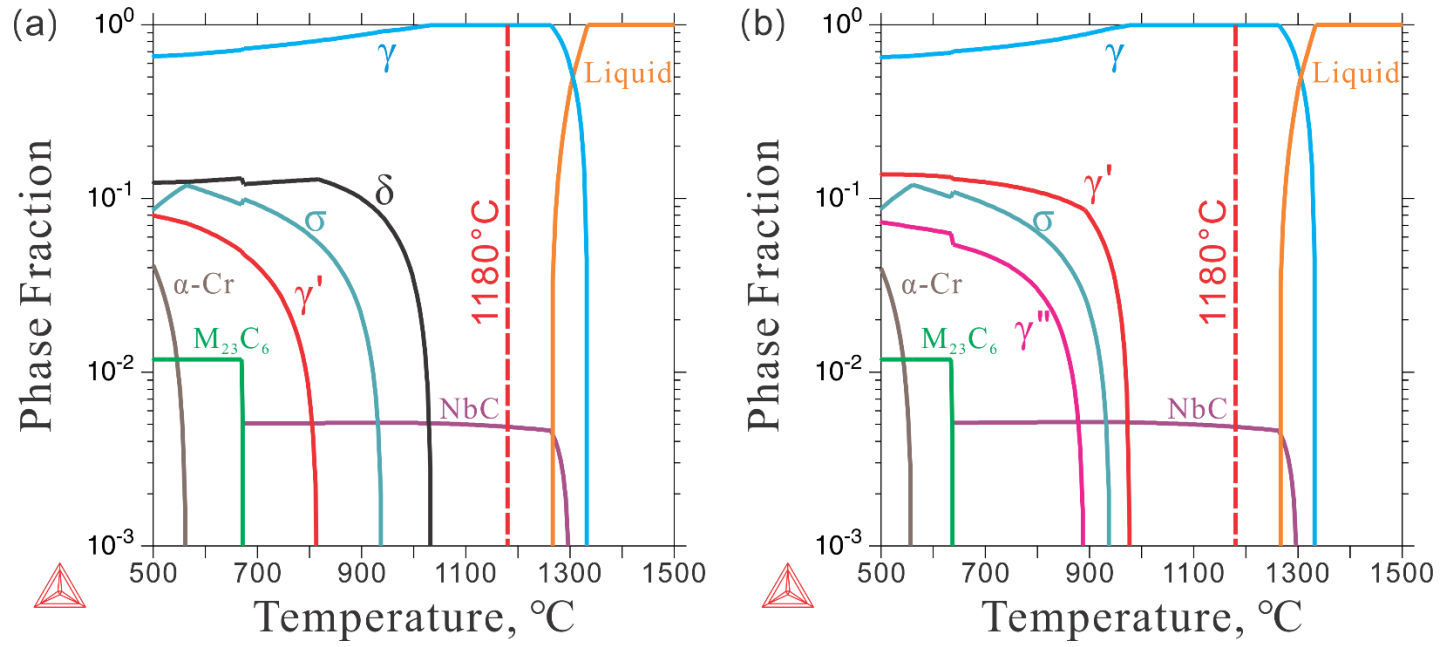


Figure 2. (a) Equilibrium step diagram of Inconel 718; (b) nonequilibrium step diagram of Inconel 718.

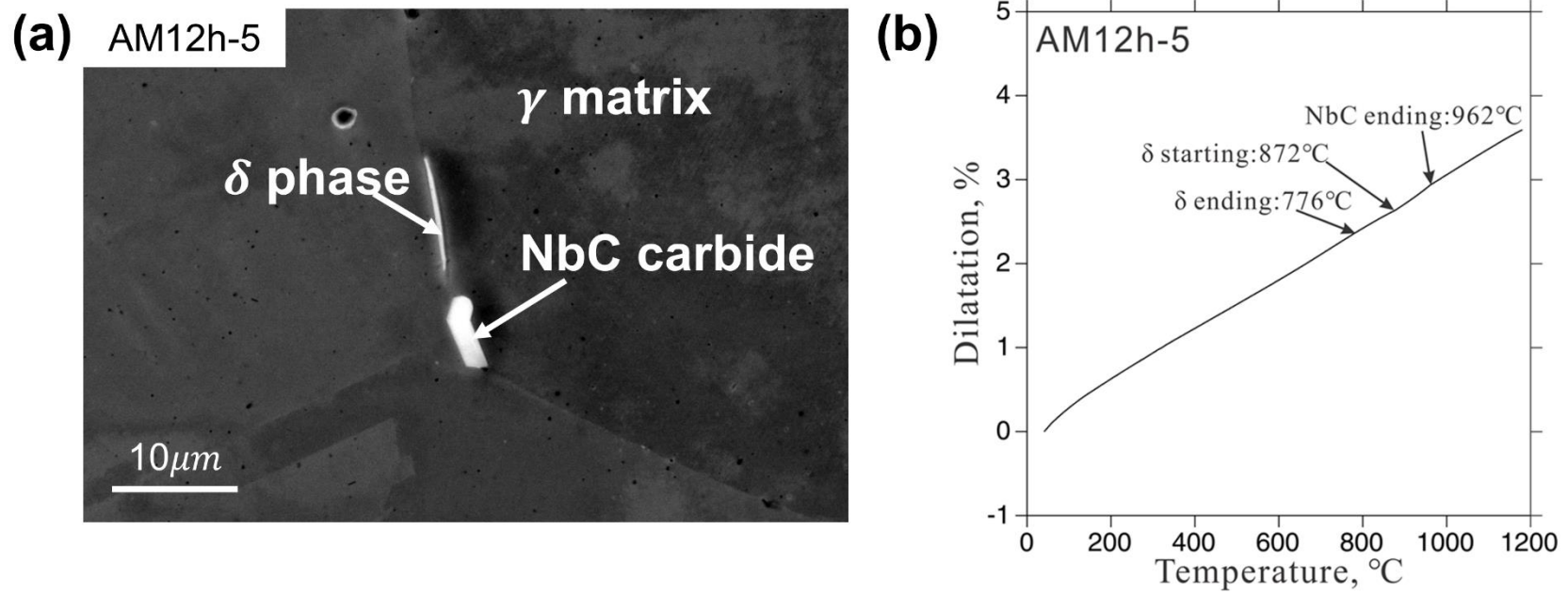


Figure 3. Microstructure characterization and dilatometry analysis of sample AM12h-5. (a) SEM micrograph on the longitudinal plane of AM12h-5; (b) dilatation curve of sample AM12h-5.

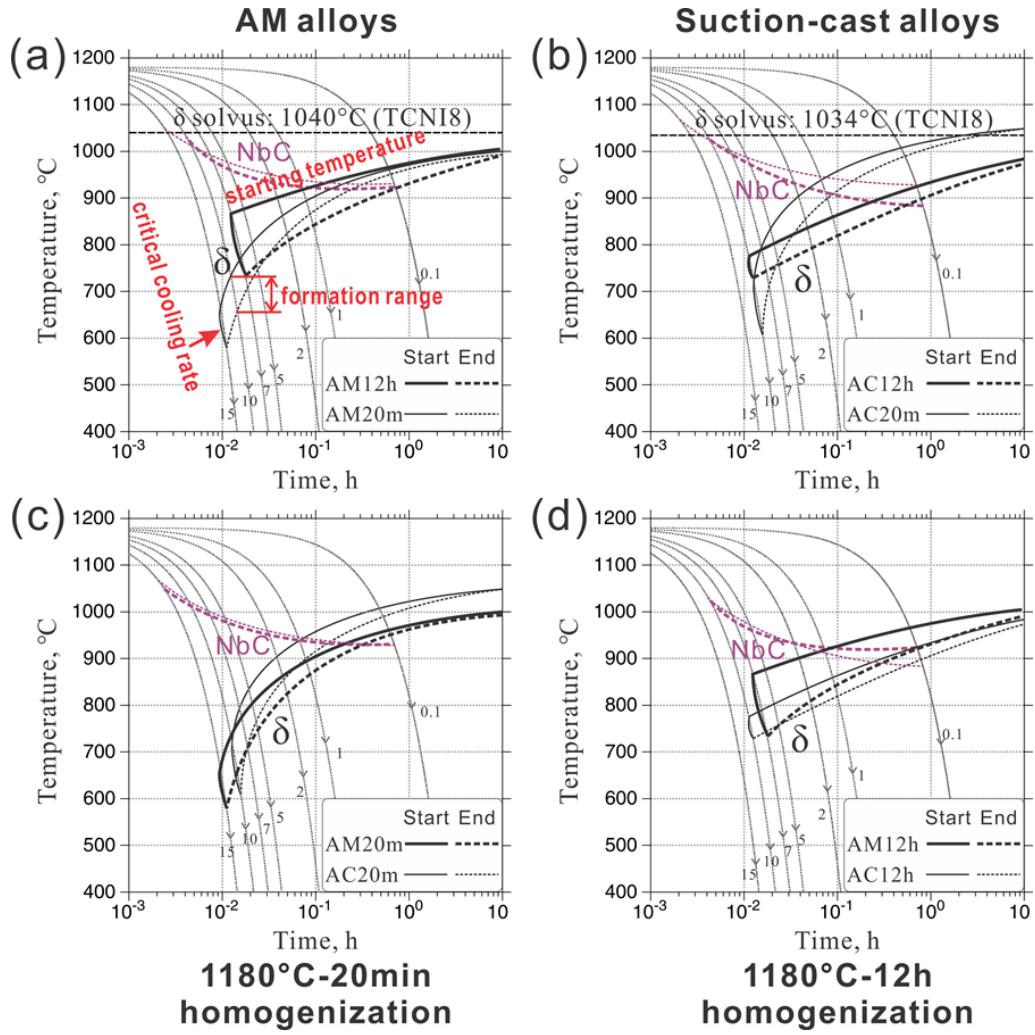


Figure 4. CCT diagrams of Inconel 718 alloys measured in the present work: (a) comparison of alloys AM12h&AM20m; (b) comparison of alloys AC12h&AC20m; (c) comparison of alloys AM20m&AC20m; (d) comparison of alloys AM12h&AC12h.

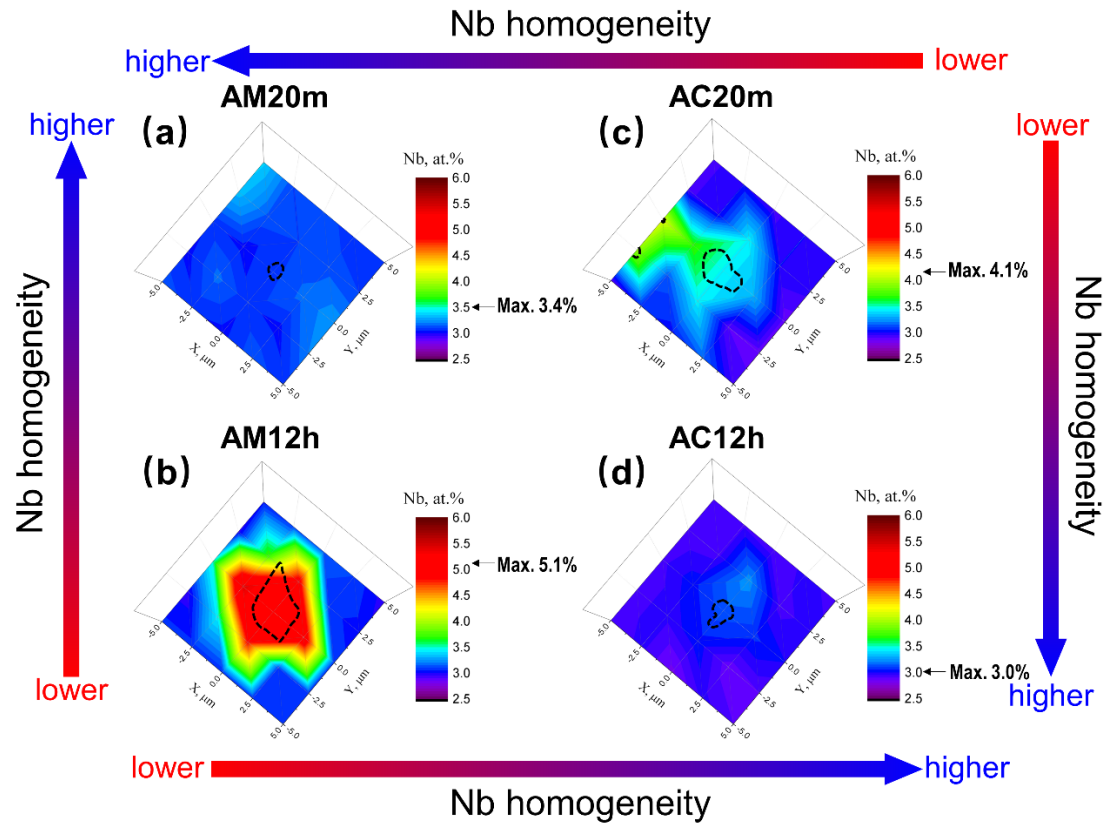


Figure 5. Illustration of Nb homogeneity evolution in additively manufactured alloys homogenized at 1180°C for (a) 20 min, AM20m; (b) 12 hours, AM12h. Illustration of Nb homogeneity evolution in suction-cast alloys homogenized at 1180°C for (a) 20 min, AC20m; (b) 12 hours, AC12h.

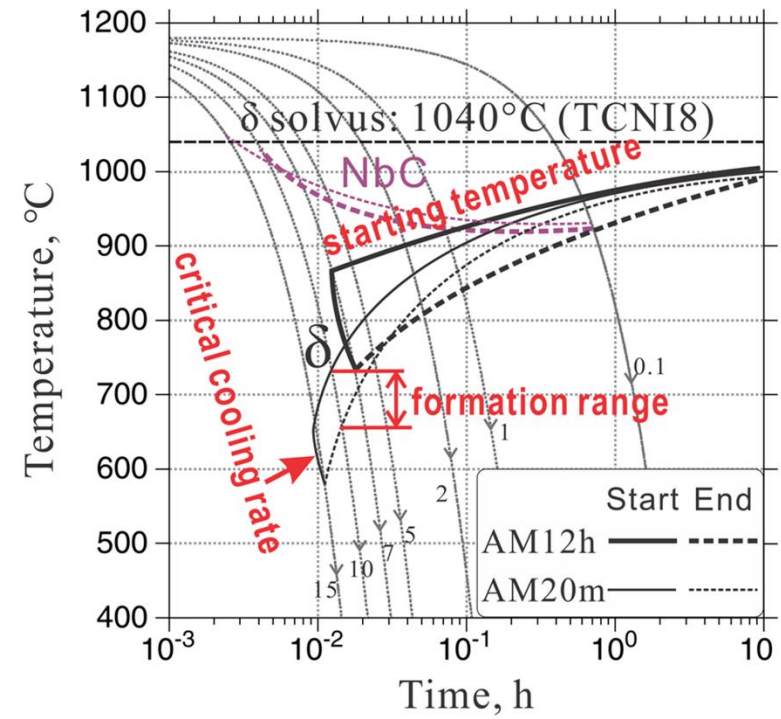
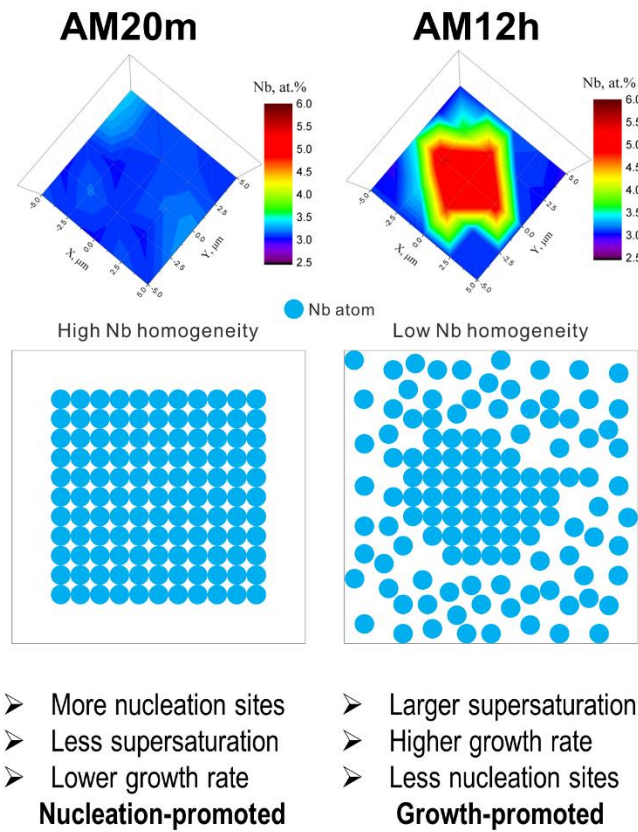


Figure 6. Illustration to the effects of Nb homogeneity on precipitation kinetics of δ phase (taking alloys AM20m and AM12h as an example).

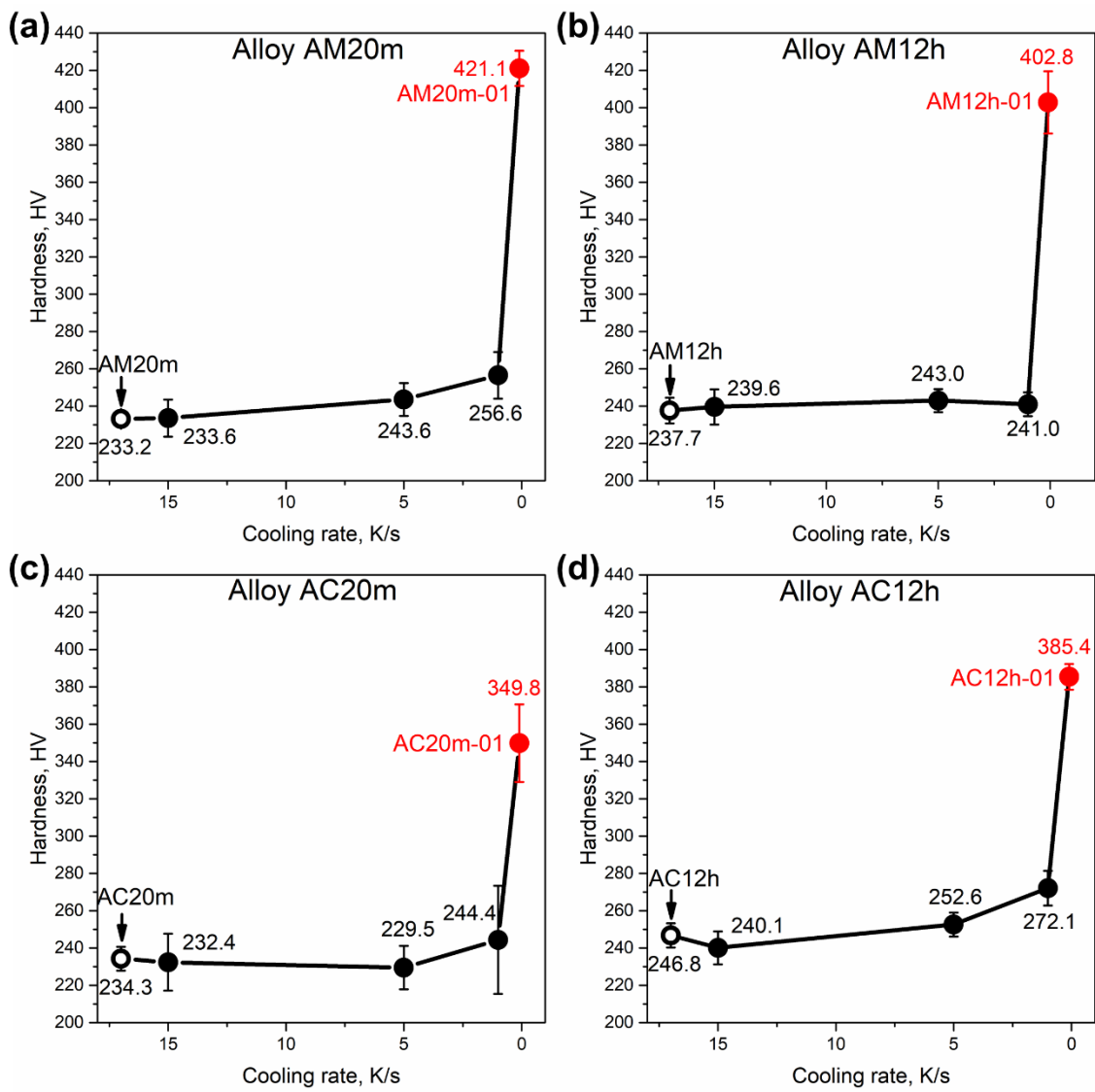


Figure 7. Vickers hardness testing results of homogenized and continuously cooled Inconel 718 samples: (a) alloy AM20m; (b) alloy AM12h; (c) alloy AC20m; (d) alloy AC12h.

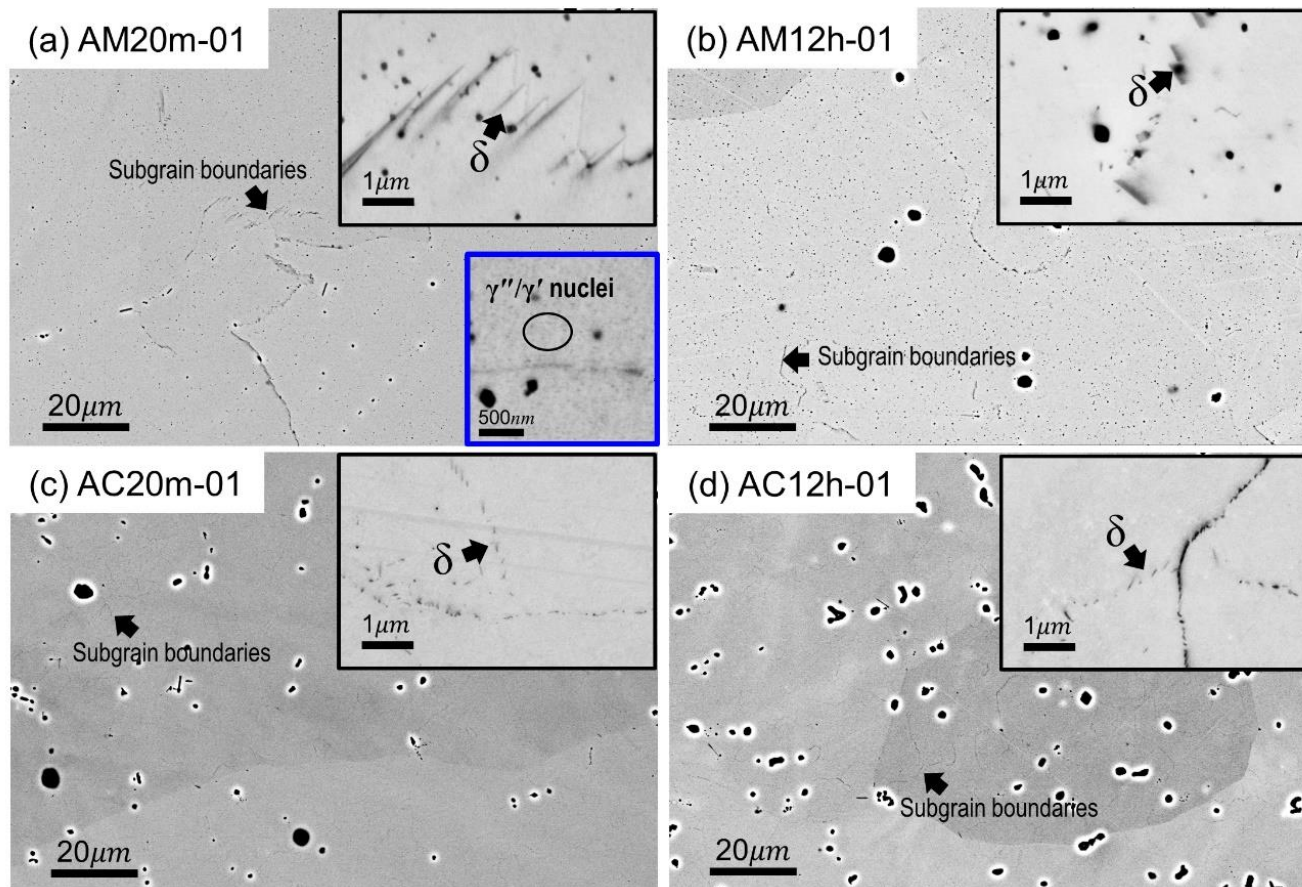


Figure 8. SEM micrographs on etched Inconel 718 samples cooled at 0.1 K/s: (a) sample AM20m-01; (b) sample AM12h-01; (c) sample AC20m-01; (d) sample AC12h-01.